

DISPERSION DIAGRAM ANALYSIS OF ARRAYS OF MULTISHELL MULTIMATERIAL NANOSPHERES

Masoud Rostami^{*}, Davood Ansari Oghol Beig,
and Hossein Mosallaei

Department of Electrical and Computer Engineering, Northeastern University, Boston, MA 02115, USA

Abstract—In this paper, the characteristics of electromagnetic waves supported by three dimensional (3-D) periodic arrays of multilayer multimaterial spheres are theoretically investigated. The spherical particles have the potential to offer electric and magnetic dipole modes, where their novel arrangements engineer the desired metamaterial performance. Multilayer spheres are designed for controlling both electric and magnetic Mie scattering resonances around the same spectrum. A full wave spherical modal formulation is applied to express the electromagnetic fields in terms of the electric and magnetic multipole modes. Imposing boundary conditions will determine the required equations for obtaining dispersion characteristics $\omega a/2\pi c - ka/2\pi$. A metamaterial constructed from unit-cells of multilayer multimaterial sphere is created. It is demonstrated such compositions can exhibit negative-slope dispersion diagram metamaterial properties in frequency spectrums of interest, where both electric and magnetic Mie scattering resonances occur. Different coatings such as silver, gold, indium-tin-oxide (ITO), Al : ZnO, (AZO) and Ga : ZnO (GZO) are used and the operating range and the losses of the resulting metamaterials are compared. It is presented that by adding the third layer to the core-shell structure, due to increased degrees of freedom, the metamaterials operation range will be tunable to the desired frequency.

1. INTRODUCTION

Metamaterials are formed by embedding inclusions and material components in host media to achieve composite structures with

Received 17 November 2012, Accepted 17 January 2013, Scheduled 22 January 2013

^{*} Corresponding author: Masoud Rostami (mrostami@ece.neu.edu).

novel phenomena that do not occur or may not be easily available in nature [1]. There are growing attentions in this area as their electromagnetic properties are considerably different from conventional materials.

Significant amount of research has been performed to realize metamaterials for novel applications. A large variety of the physical effects associated with double and single negative metamaterials and some of their very interesting impacts have been addressed [2]. Among these interesting features are negative index and negative refraction behaviors, usually known as left handed materials (LHMs) [3]. Unique applications have been highlighted, such as phase compensation, electrically small resonators, negative angles of refraction, subwavelength waveguides with lateral dimension below diffraction limits, high-performance focusing, backward-wave media, photon tunneling and electrically small antennas [1, 3–5].

To obtain an optical metamaterial with the functionality of interest one would need to create appropriate electric and magnetic dipole modes in a building block often regarded as the unit cell [6–8]. As long as isolated plasmonic particles are involved, an analytical circuit-theory based model has been introduced by Alam et al. [9, 10] which allows for the calculation of resonant frequencies and scattering parameters. Furthermore, it has been demonstrated that dielectric spheres have the potential to offer both electric and magnetic dipole modes [8, 11]. Primarily, the electric and magnetic dipole moments are the basic foundations for making metamaterials. Novel arrangements of these dipole moments can lead to desired material properties [8]. Tailoring the appropriate dipole modes allows controlling the performance of the structure.

A unit cell composed of two different spheres with the same radii and different materials or the same dielectric materials and different radii can provide the required electric and magnetic dipole modes [6, 12, 13]. The low dielectric material of the nanospheres in optical regimes generates some difficulties in tuning optical double negative (DNG) medium. There are also other works where one set of dielectric nanoparticles has been used to accomplish the backward wave behavior in optical spectrum [7]. In such works a 3-D array of dielectric particles are used where the spheres operate in their magnetic modes and their couplings offer electric modes. Bringing the dielectric spheres close to each other, increases their electromagnetic coupling in such a way that both electric and magnetic resonances can be achieved around the same frequency region. Yet, we do not have complete control over the position of the resonances.

In this work, a multilayer sphere is used as the unit cell building

block of the structure where a core dielectric sphere is wrapped in a plasmonic material shell. Two different metals (gold and silver) are used for this coating/shell layer. Metals have traditionally been the material of choice for the building blocks of many metamaterials, but they suffer from high resistive losses — even metals with the highest conductivities, silver and gold, exhibit excessive losses at optical frequencies that restrict the development of practical devices at such frequencies. The development of new materials for low loss metamaterial components and telecommunication devices is therefore required [14]. Hence, some new materials (ITO, AZO and GZO) are used as the coating layer to investigate the performance.

It is demonstrated that this arrangement can successfully provide the required electric and magnetic modes at the frequency of interest. First, a two-layer (core-shell) sphere is designed and it is shown that by adjusting the radius of the core and the thickness of the shell the relative position of the resonances with respect to each other can be controlled. Hence, one can use the mentioned configuration to enforce overlapping electric and magnetic resonances. Adding a third layer of coating increases the system flexibility. It is illustrated that by changing the thickness of the third layer the electric and magnetic resonances can be shifted simultaneously into the desired frequency band where negative-slope dispersion behaviors can be synthesized accordingly.

We develop a theoretical approach based on dipole modes to comprehensively characterize the metamaterial performance. The technique is fast and accurate and is aimed to theoretically determine the dispersion diagrams. The proposed approach is based on the

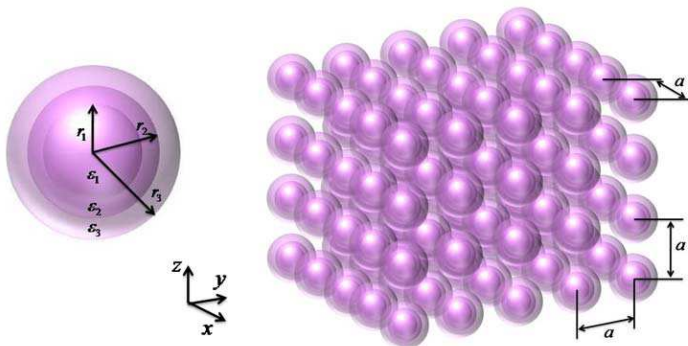


Figure 1. Configuration of an array of multimaterial multilayer spheres.

recent work by Ghadarghadr and Mosallaei [6] while it is extend to the modeling of arrays of multilayer multimaterial spheres (Figure 1). To enable this, the problem of multiple scattering of an electromagnetic plane wave by an array of spheres is solved utilizing the multipole expansion method [6, 15]. This provides an efficient theoretical model for the characterization of the periodically configured bulk of metamaterial.

2. THE THEORY AND FORMULATION

This section presents the theoretical formulation of the 3-D array of metamaterial. The building block is constructed from layered spherical particle. The Mie scattering formulation is applied to formulate the problem and solve for dispersion diagram of the periodic configuration.

2.1. Scattering Coefficients

Consider a multilayer (N layer) sphere where each layer is characterized by a relative permittivity ε_{rn} and a radius r_n , $n = 1, 2, \dots, N$. We assume the region outside the multilayer sphere is free space and the relative permeability everywhere is assumed to be $\mu_r = 1$. A plane wave excitation with x -polarized electric field and y -polarized magnetic field is considered. The field in each region can be written using the \mathbf{M} and \mathbf{N} vector basis functions [16] as:

$$\mathbf{E}_n = \sum_{m=1}^{\infty} E_m \left[c_m^{(n)} \mathbf{M}_{o1m}^{(1)} - i d_m^{(n)} \mathbf{N}_{e1m}^{(1)} + i a_m^{(n)} \mathbf{N}_{e1m}^{(3)} - b_m^{(n)} \mathbf{M}_{o1m}^{(3)} \right] \quad (1a)$$

$$\mathbf{H}_n = -\frac{k_n}{\omega \mu_0} \sum_{m=1}^{\infty} E_m \left[d_m^{(n)} \mathbf{M}_{e1m}^{(1)} + i c_m^{(n)} \mathbf{N}_{o1m}^{(1)} - i b_m^{(n)} \mathbf{N}_{o1m}^{(3)} - a_m^{(n)} \mathbf{M}_{e1m}^{(3)} \right] \quad (1b)$$

where $E_m = i^m E_0 (2m+1)/m(m+1)$, ω is the angular frequency and k_n is the angular wave number of n th layer. In (1a) and (1b), $\mathbf{M}_{o1m}^{(s)}$, $\mathbf{M}_{e1m}^{(s)}$, $\mathbf{N}_{o1m}^{(s)}$ and $\mathbf{N}_{e1m}^{(s)}$ ($s = 1, 3$) are the vector harmonic functions with the radial dependence to spherical Bessel function $j_m(kr)$ for $s = 1$ and spherical Hankel function $h_m^{(1)}(kr)$ for $s = 3$ [17].

In the region out of the sphere, the scattered field can be expanded as:

$$\mathbf{E}_{(N+1)} = \sum_{m=1}^{\infty} E_m \left[i a_m^{(N+1)} \mathbf{N}_{e1m}^{(3)} - b_m^{(N+1)} \mathbf{M}_{o1m}^{(3)} \right] \quad (2a)$$

$$\mathbf{H}_{(N+1)} = \frac{k_{(N+1)}}{\omega \mu_0} \sum_{m=1}^{\infty} E_m \left[a_m^{(N+1)} \mathbf{M}_{e1m}^{(3)} + i b_m^{(N+1)} \mathbf{N}_{o1m}^{(3)} \right] \quad (2b)$$

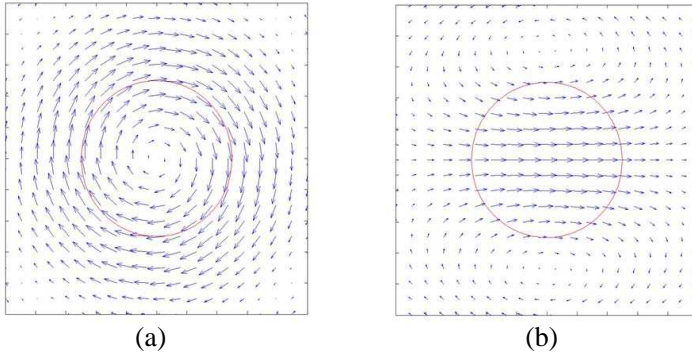


Figure 2. Vector spherical wave functions field lines. (a) \mathbf{M}_{o11} field lines. (b) \mathbf{N}_{e11} field lines.

In the section that follows, the electromagnetic fields and the Mie scattering coefficients ($a_m^{(N+1)}$ and $b_m^{(N+1)}$) are calculated by means of enforcing the tangential continuity of field components across material interfaces.

It is assumed that the dimensions of the nanospheres are sufficiently small compared to free space wavelength and hence higher order modes are neglected. The accuracy of this assumption will be discussed in Section 4.1. Therefore, the field due to each particle is modeled with dipole spherical waves. In other words, the first term of the summations (i.e., for $m = 1$) in (2a) and (2b) dominates the higher order terms and therefore scattered electric and magnetic fields outside the particle can be approximated as:

$$\mathbf{E}_{(N+1)} = \frac{-3}{2} E_0 \left[a_1^{(N+1)} \mathbf{N}_{e11}^{(3)} + i b_1^{(N+1)} \mathbf{M}_{o11}^{(3)} \right] \quad (3a)$$

$$\mathbf{H}_{(N+1)} = \frac{3k^{(N+1)}}{2\omega\mu_0} E_0 \left[i a_1^{(N+1)} \mathbf{M}_{e11}^{(3)} - b_1^{(N+1)} \mathbf{N}_{o11}^{(3)} \right] \quad (3b)$$

It is worthwhile recalling that the spherical vector wave function \mathbf{M} has a circular field pattern on the interface, i.e., $\mathbf{M} \cdot \hat{e}_r = 0$. On the contrary \mathbf{N} includes nonzero radial component. The behavior is graphically depicted in Figure 2. Looking at (3) one observes that controlling the $a_1^{(N+1)}$ and $b_1^{(N+1)}$ coefficients electric and magnetic dipole modes can be excited in the particle. For instance, if $a_1^{(N+1)}$ has a large value and $b_1^{(N+1)}$ is small, an electric dipole mode is induced and vice versa.

2.2. Electric and Magnetic Mie Scattering Coefficients

In this section the electric and magnetic Mie scattering coefficients of the multilayer sphere are obtained. Using an approach similar to that of [18] one can find the \hat{e}_θ and \hat{e}_ϕ components of the m th mode of the electric and magnetic field in region n as:

$$\begin{bmatrix} E_{n\theta}^m \\ E_{n\phi}^m \end{bmatrix} = \frac{-1}{i\omega\epsilon_n} \begin{bmatrix} \frac{\partial}{\partial\theta} P_m^1(\cos\theta) \\ \frac{i}{\sin\theta} P_m^1(\cos\theta) \end{bmatrix} \cdot \left[\tilde{U}_{n,n-1} \frac{1}{r} \frac{\partial}{\partial r} r h_m^{(1)}(k_n r) + \frac{1}{r} \frac{\partial}{\partial r} r j_n(k_n r) \right] \cdot A_n \quad (4a)$$

$$\begin{bmatrix} H_{n\theta}^m \\ H_{n\phi}^m \end{bmatrix} = \begin{bmatrix} \frac{i}{\sin\theta} P_m^1(\cos\theta) \\ -\frac{\partial}{\partial\theta} P_m^1(\cos\theta) \end{bmatrix} \cdot \left[\tilde{U}_{n,n-1} \frac{1}{r} \frac{\partial}{\partial r} h_m^{(1)}(k_n r) + j_n(k_n r) \right] \cdot A_n \quad (4b)$$

Here, we have used Debye potentials for characterizing the scalar waves and $e^{im\phi}$ dependences are suppressed. In the above $\tilde{U}_{n,n-1}$ is the reflection from the boundary between regions $n-1$ and n considering the effect of the other inner layers. In spherically layered media, the TM^r and TE^r (transverse to \hat{e}_r) waves are decoupled and (4a) and (4b) represent either of the TM^r or the TE^r spherical modes. Now, since a standing wave in region $n-1$ is a consequence of the standing wave in region n plus the reflection of the outgoing wave in region $n-1$, one can write:

$$A_{n-1} = T_{n,n-1} A_n + R_{n-1,n} \tilde{U}_{n-1,n-2} A_{n-1} \quad (5)$$

In (5), $T_{n,n-1}$ is the transmission coefficient of incoming wave travelling from region n to $n-1$ while $R_{n-1,n}$ is the reflection without considering the effect of other layers. Hence,

$$A_{n-1} = \frac{T_{n-1,n}}{1 - R_{n-1,n} \tilde{U}_{n-1,n-2}} A_n \quad (6)$$

Furthermore, the outgoing wave in region n is just a consequence of the reflection of the standing wave in region n plus the transmission of the outgoing wave in region $n-1$, therefore,

$$\tilde{U}_{n,n-1} A_n = R_{n,n-1} A_n + T_{n-1,n} R_{n-1,n-2} A_{n-1} \quad (7)$$

Substituting A_{n-1} from (6) into (7) yields

$$\tilde{U}_{n,n-1} = R_{n,n-1} + \frac{T_{n-1,n} \tilde{U}_{n-1,n-2} T_{n,n-1}}{1 - R_{n-1,n} \tilde{U}_{n-1,n-2}} \quad (8)$$

where $\tilde{U}_{1,0} = 0$.

As mentioned earlier, these relations are valid for both TM^r and TE^r cases. Therefore, by using the general recursive relation (8) one

can find the coefficients in (2a) and (2b) by using $a_m^{(N+1)} = \tilde{U}_{N+1,N}^{TM}$ and $b_m^{(N+1)} = \tilde{U}_{N+1,N}^{TE}$. For this purpose, TM^r and TE^r reflection and transmission coefficients need to be obtained without considering the effect of other layers first. These parameters can be found by matching the boundary conditions in (4a) and (4b) for a solid sphere. Hence, the TM^r reflection and transmission coefficients are found as [18]:

$$R_{n,n-1}^{TM} = \frac{\sqrt{\varepsilon_n \mu_{n-1}} \hat{J}_m(k_n r_{n-1}) \hat{J}'_m(k_{n-1} r_{n-1}) - \sqrt{\varepsilon_{n-1} \mu_n} \hat{J}_m(k_{n-1} r_{n-1}) \hat{J}'_m(k_n r_{n-1})}{\sqrt{\varepsilon_{n-1} \mu_n} \hat{J}_m(k_{n-1} r_{n-1}) \hat{H}_m^{(1)'}(k_n r_{n-1}) - \sqrt{\varepsilon_n \mu_{n-1}} \hat{H}_m^{(1)}(k_n r_{n-1}) \hat{J}'_m(k_{n-1} r_{n-1})} \quad (9a)$$

$$T_{n,n-1}^{TM} = \frac{i \varepsilon_{n-1} \sqrt{\frac{\mu_{n-1}}{\varepsilon_n}}}{\sqrt{\varepsilon_{n-1} \mu_n} \hat{J}_m(k_{n-1} r_{n-1}) \hat{H}_m^{(1)'}(k_n r_{n-1}) - \sqrt{\varepsilon_n \mu_{n-1}} \hat{H}_m^{(1)}(k_n r_{n-1}) \hat{J}'_m(k_{n-1} r_{n-1})} \quad (9b)$$

where $\hat{J}_m(x) = x j_n(x)$ and $\hat{H}_m^{(1)}(x) = x h_m^{(1)}(x)$. The relation for $R_{n-1,n}^{TM}$ can easily be found by replacing the Riccati-Bessel functions $\hat{J}_m(x)$ in the nominator by Riccati-Hankel functions $\hat{H}_m^{(1)}(x)$ and also $T_{n-1,n}^{TM}$ can be found by changing the indices of n and $n - 1$ in the nominator [18].

The corresponding relations for the TE^r case can be easily obtained by means of electromagnetic duality theorem. Once the complete expression for $a_m^{(N+1)}$ and $b_m^{(N+1)}$ is derived, one can enforce electric and/or magnetic Mie scattering resonances by means of forcing the denominators of $a_m^{(N+1)}$ and $b_m^{(N+1)}$ to vanish.

For a two-layer sphere the first mode of electric and magnetic Mie scattering coefficients can be found from (8) as:

$$a_1^3 = \tilde{U}_{3,2}^{TM} = R_{3,2}^{TM} + \frac{T_{2,3}^{TM} R_{2,1}^{TM} T_{3,2}^{TM}}{1 - R_{2,3}^{TM} R_{2,1}^{TM}} \quad (10a)$$

$$b_1^3 = \tilde{U}_{3,2}^{TE} = R_{3,2}^{TE} + \frac{T_{2,3}^{TE} R_{2,1}^{TE} T_{3,2}^{TE}}{1 - R_{2,3}^{TE} R_{2,1}^{TE}} \quad (10b)$$

where one can write the TM^r reflection and transmission terms from (9a) and (9b) as:

$$R_{2,1}^{TM} = \frac{\sqrt{\varepsilon_2/\varepsilon_1} \hat{J}_1(k_2 r_1) \hat{J}'_1(k_1 r_1) - \hat{J}_1(k_1 r_1) \hat{J}'_1(k_2 r_1)}{\hat{J}_1(k_1 r_1) \hat{H}_1^{(1)'}(k_2 r_1) - \sqrt{\varepsilon_2/\varepsilon_1} \hat{H}_1^{(1)}(k_2 r_1) \hat{J}'_1(k_1 r_1)} \quad (11a)$$

$$R_{3,2}^{TM} = \frac{\hat{J}_1(k_0 r_2) \hat{J}'_1(k_2 r_2) - \sqrt{\varepsilon_2/\varepsilon_0} \hat{J}_1(k_2 r_2) \hat{J}'_1(k_0 r_2)}{\sqrt{\varepsilon_2/\varepsilon_0} \hat{J}_1(k_2 r_2) \hat{H}_1^{(1)'}(k_0 r_2) - \hat{H}_1^{(1)}(k_0 r_2) \hat{J}'_1(k_2 r_2)} \quad (11b)$$

$$R_{2,3}^{TM} = \frac{\sqrt{\varepsilon_3/\varepsilon_2} \hat{H}_1^{(1)}(k_3 r_2) \hat{H}_1^{(1)'}(k_2 r_2) - \hat{H}_1^{(1)}(k_2 r_2) \hat{H}_1^{(1)'}(k_3 r_2)}{\hat{J}_1(k_2 r_2) \hat{H}_1^{(1)'}(k_3 r_2) - \sqrt{\varepsilon_3/\varepsilon_2} \hat{H}_1^{(1)}(k_3 r_2) \hat{J}'_1(k_2 r_2)} \quad (11c)$$

$$T_{3,2}^{TM} = \frac{i\varepsilon_2/\varepsilon_0}{\sqrt{\varepsilon_2/\varepsilon_0} \hat{J}_1(k_2 r_2) \hat{H}_1^{(1)'}(k_0 r_2) - \hat{H}_1^{(1)}(k_0 r_2) \hat{J}'_1(k_2 r_2)} \quad (11d)$$

$$T_{2,3}^{TM} = \frac{i\varepsilon_0/\varepsilon_2}{\hat{J}_1(k_2 r_2) \hat{H}_1^{(1)'}(k_0 r_2) - \sqrt{\varepsilon_0/\varepsilon_2} \hat{H}_1^{(1)}(k_0 r_2) \hat{J}'_1(k_2 r_2)} \quad (11e)$$

As mentioned, similar relations for TE^r case can be found by duality theorem. One can also derive easily the coefficients for the three-layer case.

2.3. Effective Medium for the Array

From the obtained equations in previous section one can determine the effective medium for a 3-D array made from small scatterers. The assumption is the spheres are small in comparison to the wavelength such that effective constitutive medium properties can be defined.

In a three dimensional array of particles with volume density \tilde{N} , the effective permittivity ε_r^{eff} and permeability μ_r^{eff} can be obtained from (12a) and (12b) [19]. These relations reflect the first scattered electric and magnetic dipole sources of array particle, i.e., terms with $a_1^{(N+1)}$ and $b_1^{(N+1)}$ coefficients, to the constitutive constants of the bulk medium.

$$\varepsilon_r^{eff} = \frac{k_0^3 + 4\pi i \tilde{N} a_1^{(N+1)}}{k_0^3 - 2\pi i \tilde{N} a_1^{(N+1)}} \quad (12a)$$

$$\mu_r^{eff} = \frac{k_0^3 + 4\pi i \tilde{N} b_1^{(N+1)}}{k_0^3 - 2\pi i \tilde{N} b_1^{(N+1)}} \quad (12b)$$

Therefore, by controlling $a_1^{(N+1)}$ and $b_1^{(N+1)}$ a collection of multilayer non-magnetic spheres can be designed to yield almost arbitrary values of ε_r^{eff} and μ_r^{eff} (depending on the availability of the required materials for the sphere itself). Furthermore, structures with negative index of refraction can also be realized. This requires both permittivity and permeability coefficients to be negative. Hence, the multilayer spheres must be designed to exhibit simultaneous electric and magnetic resonances, i.e., in the Mie scattering sense, within the same frequency band.

3. DISPERSION DIAGRAM ANALYSIS

Substantial physical knowledge of the material properties of a bulk medium can be extracted from the dispersion diagram, i.e., plot of $\omega a/2\pi c$ versus $ka/2\pi$, associated with that medium. The dispersion diagram for 2-D and 3-D arrays of spheres has been previously obtained in [6,21] and here we follow a similar approach. To obtain the dispersion diagram, a plane wave excitation with x -polarized electric field and y -polarized magnetic field is considered. The electric and magnetic dipole components of each sphere are oriented in the x and y direction respectively. It is assumed that the array can support an electromagnetic plane wave with the propagation vector k which lies in the direction of array axis (z). The electric and magnetic dipole modes in the array are coupled through the fields scattered by the spheres. The dispersion relation is obtained by equating the electric (magnetic) field incident on any sphere of the array to the sum of the electric (magnetic) dipole fields scattered from all other spheres in the array. For simplicity it is assumed that the reference sphere is assumed to be centered at $(0, 0, 0)$ of the Cartesian coordinate system. Hence, the field incident on the reference sphere which is due to the field scattered from other spheres can be expressed as:

$$\mathbf{E}_0 = \sum_{l_x=-\infty}^{\infty} \sum_{\substack{l_y=-\infty \\ (l_x, l_y, l_z) \neq (0,0,0)}}^{\infty} \sum_{l_z=-\infty}^{\infty} \mathbf{E}_{l_x l_y l_z} \quad (13a)$$

$$\mathbf{H}_0 = \sum_{l_x=-\infty}^{\infty} \sum_{\substack{l_y=-\infty \\ (l_x, l_y, l_z) \neq (0,0,0)}}^{\infty} \sum_{l_z=-\infty}^{\infty} \mathbf{H}_{l_x l_y l_z} \quad (13b)$$

Here, $\mathbf{E}_{l_x l_y l_z}$ and $\mathbf{H}_{l_x l_y l_z}$ are the scattered electric and magnetic field from the element located at (l_x, l_y, l_z) . Also, from (3), the scattered field from each sphere is related to the external incident field through the Mie scattering coefficients:

$$\mathbf{E}_{l_x l_y l_z} = \frac{-3}{2} E_0 \left[a_1^{(N+1)} \mathbf{N}_{e11}^{(3)} + i b_1^{(N+1)} \mathbf{M}_{o11}^{(3)} \right] \quad (14a)$$

$$\mathbf{H}_{l_x l_y l_z} = \frac{3k^{(N+1)}}{2\omega\mu_0} E_0 \left[i a_1^{(N+1)} \mathbf{M}_{e11}^{(3)} - b_1^{(N+1)} \mathbf{N}_{o11}^{(3)} \right] \quad (14b)$$

The assumption that a dipolar travelling wave with periodic $\exp(ikz)$ dependence ($\text{real}\{k\} > 0$) can be supported by the array yields a relation for the normalized travelling wave propagation constant ka as a function of radiuses, dielectric functions and $\omega a/c$.

Using the above, the desired system of equations for extracting the dispersion relation is determined as done in [6, 20, 21]:

$$\frac{(\omega a/c)^3 - S_- \Sigma_1}{S_- \Sigma_2} = \frac{S_+ \Sigma_2}{(\omega a/c)^3 - S_+ \Sigma_1}; \quad \omega a/c < ka \quad (15)$$

Detailed definitions for $S_- = i(3/2)a_1^{(N+1)}$, $S_+ = i(3/2)b_1^{(N+1)}$, Σ_1 and Σ_2 can be found in [20].

4. PERFORMANCE ANALYSIS OF MULTILAYER SPHERES

4.1. Two-layer Structure

Two layered spheres with various types of shells are used to engineer the desired metamaterial characteristics. The material choices considered for the shell are gold, silver, ITO, AZO and GZO. In the subsections that follow, each different shell type is briefly discussed in terms of its optical properties and the design procedure aimed at obtaining simultaneous electric and magnetic Mie resonances. Envisioning DNG performance, a core material $\epsilon_{r1} = 20$ is assumed and then the core and the shell radius are engineered to exhibit a dispersion diagram with negative slope. To simplify the design procedure the core material losses are ignored. The design procedure is general and can be applied to other types of materials.

The electric and magnetic resonances coefficients are determined from (10a) and (10b), respectively. By careful look at these equations and (11a)–(11e) one can observe under the condition of small r_1 (compared to the wavelength) and low ϵ_2 (compared to the core material) for the magnetic Mie scattering coefficient (10b) $R_{3,2}^{TE}$ goes to zero and the frequency of resonance is dominantly determined by the radius of the core and is almost the frequency which the resonance of $R_{2,1}^{TE}$ occurs. For the electric Mie scattering coefficient in (10a), because of the mentioned assumptions, $R_{2,1}^{TM}$ (the only term which has dependence on r_1) is small and almost constant and thus the frequency for the resonance is strongly controlled by the thickness of the shell. Therefore one can say the magnetic resonance is mainly obtained by the core and the electric resonance by the shell.

In this work we design the multilayer spheres so that the dielectric constant of the shell at the resonance frequency is at -0.2 . The radius of the core is then found by adjusting the resonance of $R_{2,1}^{TE}$ to the desired simultaneous resonance frequency and the radius of the shell is obtained from electric Mie scattering coefficient (10a).

Here, a Drude model for the permittivity of shell is used:

$$\frac{\epsilon}{\epsilon_0} = \epsilon_\infty - \frac{\omega_p^2}{\omega(\omega + i\Gamma)} \tag{16}$$

where ω_p is plasma frequency and Γ the characteristic collision frequency. Because the metal thicknesses used in the examples here are a few nanometers, the parameters in the Drude model should be modified by considering some important effects at such length scale. The parameters for different materials used in this paper are shown in Table 1 [22]. The real and imaginary parts of the dielectric functions are respectively shown in Figures 3(a) and 3(b).

4.1.1. Gold Shell

Gold (Au) has wide applications in almost all different branches of nanotechnology. Gold plays an important role in a myriad of plasmonics-type spectroscopies — such as surface enhanced Raman scattering (SERS) — where it is widely preferred for biological applications over silver for its relatively easier surface chemistry, the possibility of attaching molecules viathiol groups, good biocompatibility, and chemical stability.

As discussed in Section 4 the core-shell design is achieved for when the shell has $\epsilon_r = -0.2$, which is where the gold material is at $f = 1575$ THz (see Figure 3(a)). Given the design frequency of 1575 THz the radius of the core is obtained at 20.7 nm and the shell radius is then obtained to be 22 nm. This design will ensure the poles

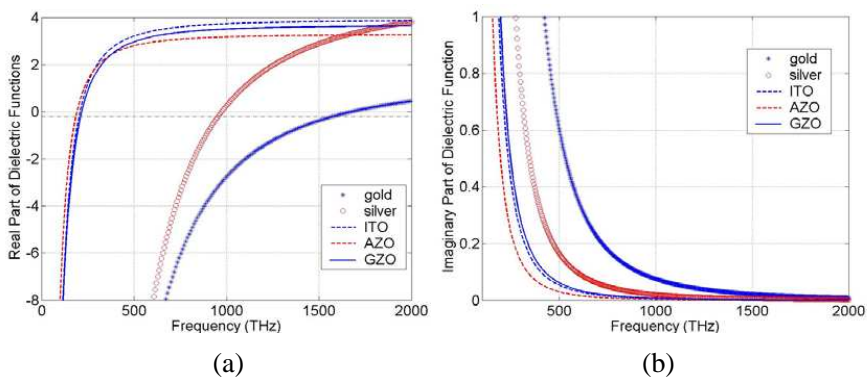
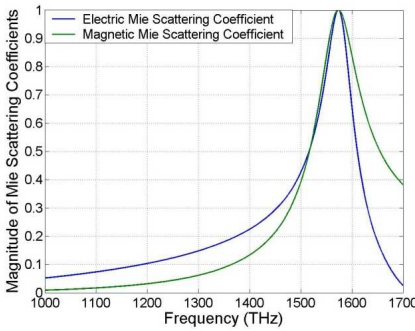
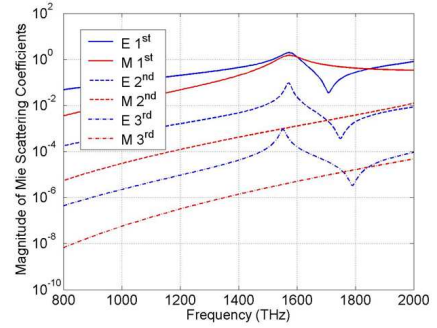


Figure 3. (a) Real and (b) imaginary parts of the Drude dielectric functions of materials used in this work.

Table 1. The Drude model parameters of different materials.

Material	ε_∞	ω_p [THz]	Γ [THz]
Gold	1.53	2069	17.64
Silver	5	2175	4.35
ITO	3.91	418.1	38.1
AZO	3.3	352.2	30.4
GZO	3.69	425.26	43

**Figure 4.** Normalized electric and magnetic Mie scattering coefficients of a single two-layer sphere for the first mode with core $\varepsilon_{r1} = 20$, $r_1 = 20.7$ nm and gold shell with $r_2 = 22$ nm.**Figure 5.** The amplitude of three first modes of electric and magnetic Mie scattering coefficients of a two-layer sphere with core $\varepsilon_{r1} = 20$, $r_1 = 20.7$ nm and gold shell with $r_2 = 22$ nm.

of the electric and magnetic Mie resonances to be around the same band (as shown in Figure 4).

As mentioned earlier, it is assumed here that the spheres are small enough so that the multipole expansion of the electric field can be approximated with the first dipole mode. The first three modes of Mie scattering coefficients for the designed two-layer sphere are presented in Figure 5 in which the strong dominance of the first mode is evident, hence validating the assumption that a single dipole mode can effectively model the problem.

Now from (4) it can be concluded that using this two-layer sphere in an array structure will lead to a DNG material. The lattice constant of the 3-D array structure presented in Figure 1 is considered as $a = 75$ nm. We apply the developed equations in Section 3 and

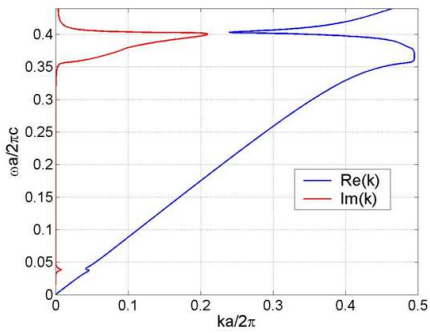


Figure 6. Real and imaginary parts of dispersion diagram for using two-layer spheres with core ($\epsilon_{r1} = 20$, $r_1 = 20.7$ nm) and gold shell with $r_2 = 22$ nm in array structure of Figure 1 with unit cell $a = 75$ nm.

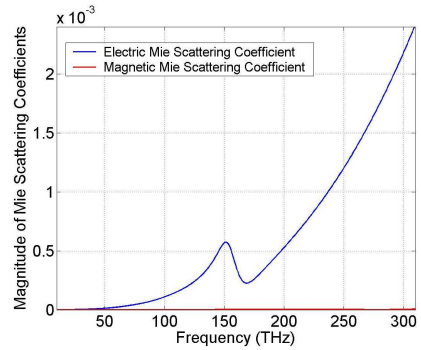


Figure 7. Electric and magnetic Mie scattering features at the lower frequency 160 THz. The core is dielectric with $\epsilon_{r1} = 20$, $r_1 = 20.7$ nm and the shell is gold with $r_2 = 22$ nm.

obtain the dispersion diagram as plotted in Figure 6. In this figure, one observes a frequency band where slope of the real part of the dispersion diagram is negative. As expected from the design, the negative slope frequency band is centered at about $\omega a/2\pi c = 0.39$ which corresponds 1560 THz. Therefore, in this band the group and phase velocities are oriented along opposite directions resulting in a so called backward wave. The obtained lattice constant is not quite in subwavelength region. Using a higher dielectric material for core can overcome this problem (though the availability of material in this frequency band can be a challenge). Also, from Figure 6 it is evident that the imaginary part of the propagation vector has close to zero values everywhere except around resonance. The maximum value of tangent loss is $\text{Im}(ka) = 1.32$ which clearly shows the lossy behavior of the negative-slope region.

In Figure 6, a small feature is observed at about $\omega a/2\pi c = 0.04$ which corresponds to $f \approx 160$ THz. A quick glance at the Mie scattering coefficients, as depicted in Figure 7, reveals that the tiny feature in Figure 6 is due to the small local maxima of the electric Mie scattering coefficient at the proximity of 160 THz.

The design procedure discussed in this subsection is almost identically repeated for the other shell types, i.e., silver, ITO, AZO and GZO. Hence, in what follows, it suffices to report the resulting dispersion diagrams and design parameters.

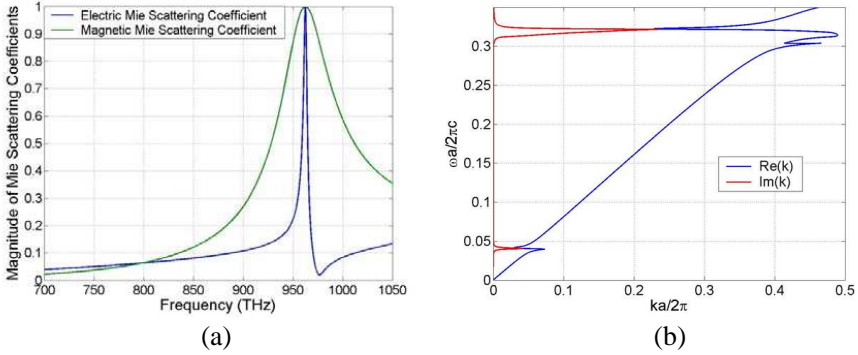


Figure 8. (a) Normalized electric and magnetic Mie scattering coefficients of a single two-layer sphere with silver shell, and (b) real and imaginary parts of dispersion diagram for the element used in array structure of Figure 1 with unit cell $a = 100$ nm ($r_1 = 33.77$ nm and $r_2 = 35$ nm).

4.1.2. Silver Shell

Silver (Ag) has the highest electrical conductivity among natural elements and the highest thermal conductivity among metals. In fact, silver nanoparticles can have effective extinction (scattering plus absorption) cross sections up to ten times larger than their physical cross section [23].

From Figure 3(a) the -0.2 permittivity for silver occurs at frequencies slightly below 960 THz. Hence, following the same procedure as in the previous subsection, the radius of the core and the thickness of the shell are respectively determined to be 33.77 nm and 1.23 nm. Scattering coefficients for this design are presented in Figure 8(a).

The designed two-layer sphere is used to construct a 3-D array structure with a lattice constant of $a = 100$ nm. The real and imaginary parts of the resultant dispersion diagram are computed and presented in Figure 8(b). The range with negative real part slope is found to be centered at around $\omega a / 2\pi c = 0.32$ which corresponds to frequencies about 960 THz (close to resonance frequency in Figure 8(a)). The maximum loss occurs in resonance region and is $\text{Im}(ka) = 1.445$.

Comparison of Figure 6 and Figure 8(b) shows that although the plasma frequencies of silver and gold in their Drude model are close to each other but there is a large difference in resonances frequencies

where negative slope occurs. This difference comes from the difference in the frequency which satisfies the design condition enforced on the permittivity of the shell layer (i.e., $\epsilon_r = -0.2$). This frequency for gold is about 1575 THz while for silver is about 960 THz.

As alternatives to conventional metals, new plasmonic materials offer many advantages in fields of plasmonics and metamaterials. These advantages include low intrinsic loss, semiconductor-based design, compatibility with standard nanofabrication processes, and tunability. Transparent conducting oxides such as Al : ZnO (AZO), Ga : ZnO (GZO) and indium-tin-oxide (ITO) enable many high-performance metamaterial devices [24]. In the following subsections these materials are used for shell layer of the two-layer spheres.

4.1.3. ITO Shell

ITO is used for various optical coatings, most notably infrared-reflecting coatings (hot mirrors) for automotive, sodium vapor lamp glasses, gas sensors, antireflection coatings, electrowetting on dielectrics, and Bragg reflectors for VCSEL lasers [25].

Using the $\epsilon_r = -0.2$ rule of thumb and Figure 3(a), the resonant frequency is found to be around 200 THz. The radius of dielectric core is found to be 166.6 nm and the thickness of the ITO shell is obtained as 34.4 nm. The computed Mie scattering coefficients are shown in Figure 9(a) where the resonances occur at 196.88 THz.

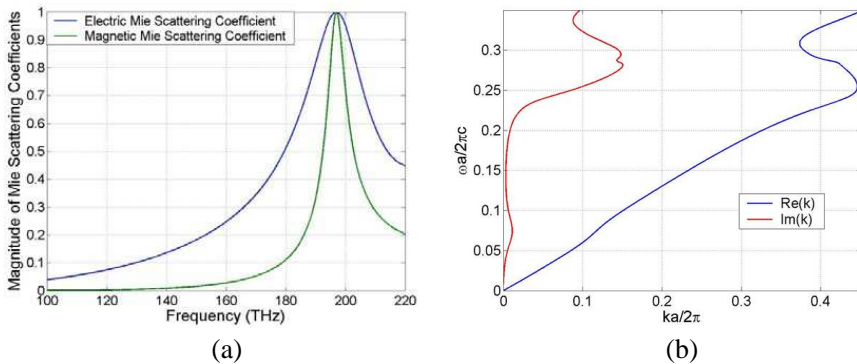


Figure 9. (a) Normalized electric and magnetic Mie scattering coefficients of a single two-layer sphere with ITO shell, and (b) real and imaginary parts of dispersion diagram for the element used in the array structure with unit cell $a = 450$ nm ($r_1 = 166.6$ nm and $r_2 = 201$ nm).

The real and imaginary parts of the dispersion diagram when using the 3-D array with an array constant of $a = 450$ nm are shown in Figure 9(b). The frequency band with negative group velocity is around $\omega a/2\pi c = 0.29$. This band is again around the resonance frequency. From the imaginary part, the loss away from the resonance frequency is small but it is not as small as in the cases with metal shell and maximum loss occurs at $\text{Im}(ka) = 0.94$. The maximum loss in negative slope region is expectedly smaller than the cases with metal shells.

4.1.4. AZO Shell

ZnOs have high transparency in the visible and near-ultraviolet spectral regions, wide conductivity range and conductivity changes under photoreduction/oxidation conditions. It has wide applications in chemical sensors, heterojunction solar cells, electrophotography, surface acoustic wave devices, conductive transparent conductors and many others. Polycrystalline ZnO films doped with group II and group III metal ions such as indium (In), aluminum (Al), gallium (Ga), copper (Cu) and cadmium (Cd) have enhanced structural, optical and electrical properties. Doping is particularly done to get high transparency, stability and high conductivity. Aluminum doping is particularly suitable for this purpose. Aluminum doped ZnO (AZO) thin films have high transmittance in the visible region, and a low resistivity and the optical band gap can be controlled by using the amount of Al doping. As a result, AZOs have potential applications in solar cells, antistatic coatings, solid-state display devices, optical

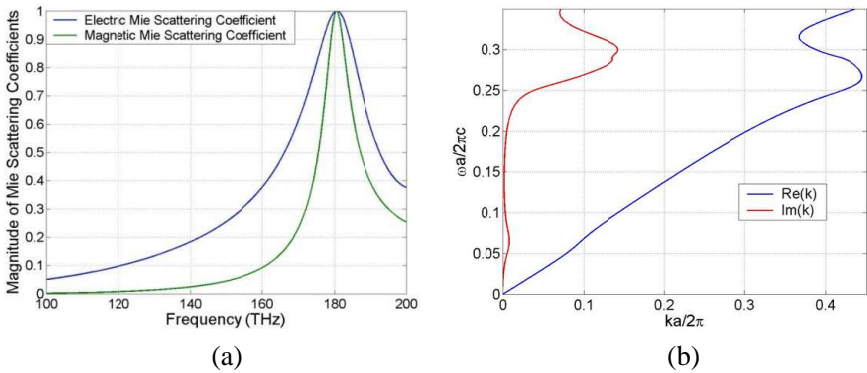


Figure 10. (a) Normalized electric and magnetic Mie scattering coefficients of a single two-layer sphere with AZO shell, and (b) real and imaginary parts of dispersion diagram for the element used in the array structure with unit cell $a = 500$ nm ($r_1 = 181.5$ nm and $r_2 = 212$ nm).

coatings, defrosters, chemical sensors etc. [26].

The design of simultaneous resonances two-layer sphere with AZO shell leads to $r_1 = 181.5 \text{ nm}$ and $r_2 = 212 \text{ nm}$. The computed Mie scattering coefficients for this two-layer sphere are presented in Figure 10(a) where the resonances occur at 180.4 THz.

Corresponding dispersion diagrams when using this two-layer sphere in the 3-D array structure with lattice constant of $a = 500 \text{ nm}$ are plotted in Figure 10(b). From the real part it is determined that the negative group velocity band is centered at $\omega a/2\pi c = 0.3$. Furthermore, from the imaginary part the losses are found to be small when operated at frequencies far from the resonance frequency. The maximum loss occurs at $\text{Im}(ka) = 0.85$ which (as expected) is smaller than that of the ITO shell case.

4.1.5. GZO Shell

Gallium doped ZnO (GZO) is another family of materials that has many applications in electronics and optics. GZOs have applications in organic light emitting diodes, solar cells, solid-state display devices mainly because of their high transparency, stability and high conductivity.

The simultaneous resonances with the GZO shell is achieved with $r_1 = 160 \text{ nm}$ and $r_2 = 194 \text{ nm}$. The computed Mie scattering coefficients are presented in Figure 11(a). The resonances occur at 205.2 THz. Dispersion diagrams for the resulting 3-D array structure with an array constant of 450 nm are plotted in Figure 11(b). The

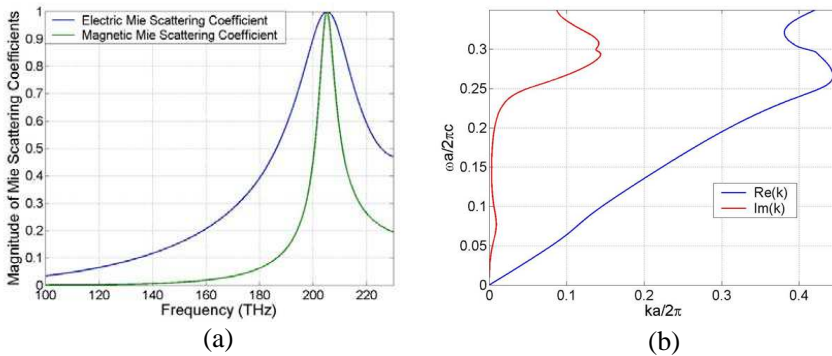


Figure 11. (a) Normalized electric and magnetic Mie scattering coefficients of a single two-layer sphere with GZO shell, and (b) real and imaginary parts of dispersion diagram for the element used in the array structure with unit cell $a = 450 \text{ nm}$ ($r_1 = 160 \text{ nm}$ and $r_2 = 194 \text{ nm}$).

range with negative group velocity is centered on about $\omega a/2\pi c = 0.3$. The loss away from the resonance frequency is small and maximum loss occurs at $\text{Im}(ka) = 0.9$ which is close to the resonances.

4.2. Three Layer Structure

As discussed in previous sections, two-layer spheres can be designed for obtaining simultaneous resonances, i.e., electric and magnetic resonances occurring at the same frequency. It is obvious from the design procedure that we do not have much control over the resonant frequency of the two layer structure. In other words, it is hard to transfer the resonance to an arbitrary frequency of choice. Hence, another dielectric layer is added to the system to increase the degrees of freedom in the location of the resonance. The third layer is made from the same dielectric material as the core ($\varepsilon_{r1} = \varepsilon_{r3} = 20$). It is found that increasing the thickness of the third dielectric layer will result in a red shift for both electric and magnetic Mie resonances. Unfortunately, though, the electric and the magnetic resonances do not experience the same shifts when the third (dielectric) layer is added to the unit cell. This mismatch is, however, easily compensated by a fractional change in the radius of the core and/or the thickness of the shell.

Here a three layer case of dielectric-gold-dielectric is explored. Recall for the two layer design that the resonances occurred at 1575 THz. Suppose a resonance frequency band around 900 THz is

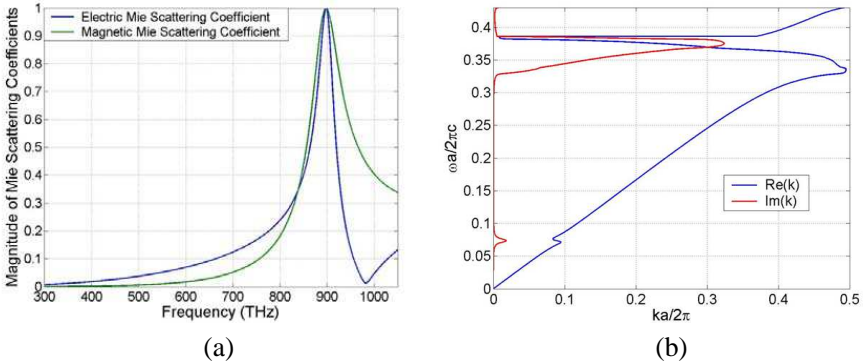


Figure 12. (a) Normalized electric and magnetic Mie scattering coefficients of a single three-layer sphere with $\varepsilon_{r1} = \varepsilon_{r3} = 20$, $r_1 = 25$ nm, $r_3 = 39.9$ nm, and region 2 is gold with $r_2 = 29$ nm, and (b) real and imaginary parts of dispersion diagram for the element used in the array structure with unit cell $a = 120$ nm.

desired. Then, adding the coating dielectric layer and adjusting its thickness, the resonance frequency can be transferred to the desired band. The objective can be achieved with $r_1 = 25$ nm, $r_2 = 29$ nm and $r_3 = 39.9$ nm for which the resonances occur at 898.1 THz. Mie coefficients for this sphere are plotted in Figure 12(a).

This three layer unit cell is integrated into the 3-D array of Figure 1 and the resulting dispersion diagram is depicted in Figure 12(b). Here, an array constant of $a = 120$ nm is considered. The negative group velocity is found to occur at frequency close to $\omega a/2\pi c = 0.36$. Similar to the two layer case with metal shells, the loss is negligible when operating at frequency away from the resonance. Maximum loss occurs at $\text{Im}(ka) = 2.07$ which is larger than the losses for the 3-D consisting of two-layer sphere unit cells.

In the end, all of the designs are summarized in Table 2. Two-layer spheres with different shell materials can be compared for their characteristic parameters, i.e., the radius of the core (r_1), the radius of the shell (r_2), the lattice constant of the 3-D array (a), the resonance frequency (ω_r) and the maximum value of $\text{Im}(ka)$. The parameters for the designed three-layer sphere are also added to the table. Using Table 2, a resonance frequency of 1500 THz can be achieved with the two-layer core-shell with gold used for the shell layer. On the other hand, if a resonance at 900 THz is desired, one option can be using silver as the shell of a two-layer sphere and the other option is using a three-layer sphere with gold as the second layer. The advantage of using the three-layer sphere lies in the controllability of the resonance frequency such that the resonance can be tuned exactly at the desired frequency at the expense of slight increase in the losses when compared to the two-layer spheres.

If the desired frequency band is about 200 THz, depending on the application, each of the ITO, AZO or GZO shell two-layer spheres can

Table 2. Designed two and three layer spheres parameters.

Shell	r_1 [nm]	r_2 [nm]	a [nm]	ω_r [THz]	Max[Im(ka)]
Gold	20.7	22	75	1575	1.32
Silver	33.77	35	100	960	1.445
ITO	166.6	201	450	196.88	0.94
AZO	181.5	212	500	180.4	0.85
GZO	160	194	450	205.2	0.9
3-Layer 2nd layer: Gold $r_3 = 39.9$ nm	25	29	120	898.1	2.07

be used. For instance, in applications like precisely etching, which the resolution is important, ITO can be used but if a lower control is enough AZO can be used instead.

It must be mentioned that the focus of this work has been on theoretical-computational analysis, and the fabrication challenges will be obviously of importance too. This will include availability of the core dielectric material and the feasibility of the required shell thickness for realization.

Also, to have a metamaterial performance a smaller lattice constant is preferable which can be achieved using higher dielectric material for the core (that can be more difficult to realize). The lattice constants used in the presented results in this work fall in the 0.3λ to 0.4λ range. Hence, from the view point of homogenization, we may consider them more like negative slope media than DNG materials.

5. CONCLUSIONS

In this paper, electromagnetic characteristics of periodic arrays of multilayer multimaterial spheres are theoretically investigated. The focus is on two aspects; first on how to design multilayer spheres that exhibit electric and magnetic Mie scattering resonances around the same frequency, and second to integrate the designed unit cells into a 3-D array configuration to achieve DNG metamaterial with negative-slope dispersion characteristic. A full wave spherical modal analysis is applied to express the electromagnetic fields in terms of the electric and magnetic multipole modes. The dispersion diagrams are obtained using a method that characterizes the interactions of electromagnetic waves with the 3-D arrays of spheres. It is assumed that the spheres are sufficiently small compared to the operating wavelength such that only the first order vector spherical waves, i.e., the dipolar modes, can sufficiently characterize the scattering effects. The dispersion diagrams for 3-D array configurations consisting of various two-layer spheres are fully characterized. It is illustrated that in an array of multilayer spheres one can combine the electric and magnetic modes properly and creates negative slope dispersion diagrams. Different metal and semiconductor materials are used for the shell layer to control the location of the DNG region and the loss performance of the resulting material. Smaller loss characteristics are achieved using ITO, AZO and GZO nonmetallic plasmonic materials. Also, it is shown the resonance frequency can be further controlled by means of replacing the two layer spherical structure with that of an alternative three layer structure. Future works will focus on achieving wider DNG operation bandwidths and smaller losses in the DNG region.

ACKNOWLEDGMENT

The authors are grateful to the US Air Force Office of Scientific Research (AFOSR) Grant No. FA9550-10-1-0438, for the support of this work.

REFERENCES

1. Engheta, N. and R. W. Ziolkowski, *Metamaterials: Physics and Engineering Explorations*, Wiley, New York, 2006.
2. Engheta, N. and R. W. Ziolkowski, "A positive future for double-negative metamaterials," *IEEE Trans. Microwave Theory Tech.*, Vol. 53, No. 4, 1535–1556, 2005.
3. Pendry, J. B., "Negative refraction makes a perfect lens," *Phys. Rev. Lett.*, Vol. 85, 3966, 2000.
4. Fang, N., H. Lee, C. Sun, and X. Zhang, "Sub-diffraction-limited optical imaging with a silver superlens," *Science*, Vol. 308, 534–537, 2005.
5. Luo, C., S. G. Johnson, J. D. Joannopoulos, and J. B. Pendry, "Subwavelength imaging in photonic crystals," *Phys. Rev. B*, Vol. 68, 045115, 2003.
6. Ghadarghadr, S. and H. Mosallaei, "Dispersion diagram characteristics of periodic array of dielectric and magnetic materials based spheres," *IEEE Trans. Antennas Propag.*, Vol. 57, No. 1, 149–160, 2009.
7. Ghadarghadr, S. and H. Mosallaei, "Coupled dielectric nanoparticles manipulating metamaterials optical characteristics," *IEEE Trans. Nanotechnol.*, Vol. 8, No. 5, 582–594, 2009.
8. Ahmadi, A. and H. Mosallaei, "Physical configuration and performance modeling of all-dielectric metamaterials," *Phys. Rev. B*, Vol. 77, 045104, 2008.
9. Alam, M. and Y. Massoud, "A closed-form analytical model for single nanoshells," *IEEE Trans. Nanotechnol.*, Vol. 5, No. 3, 265–272, May 2006.
10. Alam, M. and Y. Massoud, "RLC ladder model for scattering in single metallic nanoparticles," *IEEE Trans. Nanotechnol.*, Vol. 5, No. 5, 491–498, Sep. 2006.
11. Startton, J. A., *Electromagnetic Theory*, McGraw Hill, New York, 1941.
12. Vendik, O. G. and M. S. Gashinova, "Artificial double negative (DNG) media composed of two different dielectric sphere lattices

- embedded in a dielectric matrix,” *34th Eur. Microw. Conf.*, 1209–1212, 2004.
13. Vendik, I. B., O. G. Vendik, and M. S. Gashinova, “Artificial dielectric medium possessing simultaneously negative permittivity and magnetic permeability,” *Tech. Phys. Lett.*, Vol. 32, No. 5, 429–433, 2006.
 14. Boltasseva, A. and H. A. Atwater, “Low-loss plasmonic metamaterials,” *Science*, Vol. 331, No. 6015, 290–291, 2011.
 15. Jackson, J. D., *Classical Electrodynamics*, Wiley, New York, 1999.
 16. Yang, W., “Improved recursive algorithm for light scattering by a multilayered sphere,” *Applied Optics*, Vol. 42, No. 9, 1711–1720, 2003.
 17. Bohren, C. F. and D. R. Huffman, *Absorption and Scattering of Light by Small Particles*, Wiley, New York, 1998.
 18. Chew, W. C., *Waves and Fields in Inhomogeneous Media*, IEEE Press, 1995.
 19. Wheeler, M. S., J. S. Aitchison, and M. Mojahedi, “Coated nonmagnetic spheres with a negative index of refraction at infrared frequencies,” *Phys. Rev. B*, Vol. 73, 045105, 2006.
 20. Shore, R. A. and A. D. Yaghjian, “Traveling electromagnetic waves on linear periodic arrays of lossless spheres,” *Electronics Letters*, Vol. 41, No. 10, 578–580, 2005.
 21. Shore, R. A. and A. D. Yaghjian, “Traveling waves on two- and three-dimensional periodic arrays of lossless scatterers,” *Radio Sci.*, Vol. 42, No. 6, 2007, Doi:10.1029/2007RS003647.
 22. Alù, A., M. E. Young, and N. Engheta, “Design of nonfilters for optical nanocircuits,” *Phys. Rev. B*, Vol. 77, 144107, 2008.
 23. Li, W. R., X. B. Xie, Q. S. Shi, H. Y. Zeng, Y. S. Ouyang, and Y. B. Chen, “Antibacterial activity and mechanism of silver nanoparticles on *Escherichia coli*,” *Appl. Microbiol. Biotechnol.*, Vol. 85, No. 4, 1115–1122, 2010.
 24. Naik, G. V., J. Kim, and A. Boltasseva, “Oxides and nitrides as alternative plasmonic materials in the optical range,” *Optical Materials Express*, Vol. 1, No. 6, 1090–1099, 2011.
 25. Kim, H., J. S. Horwitz, A. Piqué, C. M. Gilmore, and D. B. Chrisey, “Electrical and optical properties of indium tin oxide thin films grown by pulsed laser deposition,” *Appl. Phys. A*, Vol. 69, S447–S450, 1999.
 26. Mondal, S., K. P. Kanta, and P. Mitra, “Preparation of Al-doped ZnO (AZO) thin film by SILAR,” *Journal of Physical Sciences*, Vol. 12, 221–229, 2008.